Table of Contents

I. Methods

a. Materials

Chromophore structures are shown in Figure 1. IR-1061(**1**) was purchased from Sigma Aldrich. IR-26 (**2**) was purchased from Exciton. Dichloromethane (DCM, HPLC grade), ethanol (anhydrous) and ethanol-d1 (99.5%) were purchased from Fisher scientific. IR-27 (**4**) and dyes **3**–**4**, **7**–**15**;[1] and **5**–**6** and **16**–**21**[2] were prepared following reported procedures.

b. Absorption coefficient

Absorption coefficients were calculated with serial dilutions in DCM in volumetric glassware. Error was taken as the standard deviation of the triplicate measurement. Absorbance spectra were collected on a JASCO V-770 UV-VIS/NIR spectrophotometer. The total molar absorption coefficient was numerically integrated over the NIR/SWIR absorption.

To find the integrated absorption cross section of the $S_0 \rightarrow S_1$ electronic state including its vibrational progression (Figure 1) in units of absorption ($\sigma(\omega)$) per unit angular frequency we numerically integrate using linear interpolation and Simpson's rule (Equation S1).

$$\int_{x_0}^{x_N} f(x)dx \approx \frac{x_n - x_o}{3n} \sum_{i=1}^{n/2} f(x_{2i-2}) + f(x_{2i-1}) + f(x_{2i}) \tag{S1}$$

Standard error was calculated by repeating this method for the upper bound and lower bound of each point from repeat measurements. The number of points used for the interpolation was twice that of the original points in that range.

c. Fluorescence quantum yield

Photoluminescence spectra were obtained on a Horiba Instruments PTI QuantaMaster Series fluorometer with 90º collection. For dyes **1**–**16**, relative quantum yields were taken with IR-26 as the standard in DCM (detailed methodology in references).[1,2] The Φ_F of IR-26 (**2**) was taken to be 5×10^{-4} in accordance with several recent measurements.[3–5] Dyes **17**–**21** were found using absolute quantum yield with an integrating sphere.[2] Quantum yield for **3'** and **3''** were determined using the relative method compared to **3** [Φ_F= $(0.61 \pm 0.02) \times 10^{-2}$].[2] For each compound, five solutions and a solvent blank were prepared and measured for their absorbance (890 nm) and emission spectra (excitation: 890 nm, emission collected between 920 – 1500 nm, no filter, excitation slit width: 0.77 nm, emission slit width: 11.52 nm, integration time: 0.3 s, step size: 4 nm) to plot integrated fluorescence intensity versus absorbance. Error calculation of quantum yield was propagated from the error in slope of both the reference and the unknown.

d. Time correlated single photon counting

We recorded PL lifetimes using a home-built, all-reflective epifluorescence setup.[6] For dyes **1**–**15**, we used a pulsed 970 nm ($70\frac{\mu J}{cm^2}$, $\mathrm{IRF} = 44 \pm 1$ ps) excitation; for dyes **16**–**20**, we used a pulsed 780 nm ($900\frac{\mu J}{cm^2}, IRF = 59 \pm 1$ ps) excitation; for the comparison of dye **3**, **3'**, **3''** we used a pulsed 785 nm ($0.19\frac{\mu J}{cm^2}, IRF = 68 \pm 1$ ps) excitation. Emission was then collected and filtered with a 90:10 beamsplitter and appropriate excitation filters finally reflectively coupled into a single-mode fiber (F-SMF-28-C-10FC, Newport) and detected using an SNSPD (Quantum Opus One).[2,6,7]

Given the short lifetimes of these dye, lifetimes were fit with a convolution of the instrument response function and an exponential. To determine the lifetime (or decay rate, k) for each TCSPC trace we fit each curve to a convolution of Gaussian with a single exponential decay:

$$I(t) = \frac{I_0}{2} e^{-k\left((t-t_0)-\frac{\sigma^2 k}{2}\right)}\left(1+\operatorname{erf}\left(\frac{(t-t_0)-\sigma^2 k}{\sqrt{2}\sigma}\right)\right) \qquad \text{(S2)}$$

The width, σ, of the Gaussian was determined using the instrument response function (IRF) which was measured as the back-scatter off of a cuvette with solvent (i.e. DCM) without the longpass filters. The initial peak amplitude, I_0, and the rate, k, were free fitting parameters, while the time offset, t_0, and the IRF width, σ were fixed variables. We use a conservative error of 1 ps (the instrument resolution) for our lifetimes except where noted in our statistics. Figure S1 shows the lifetime fitting of the Dye **3**, **3'**, **3"**.

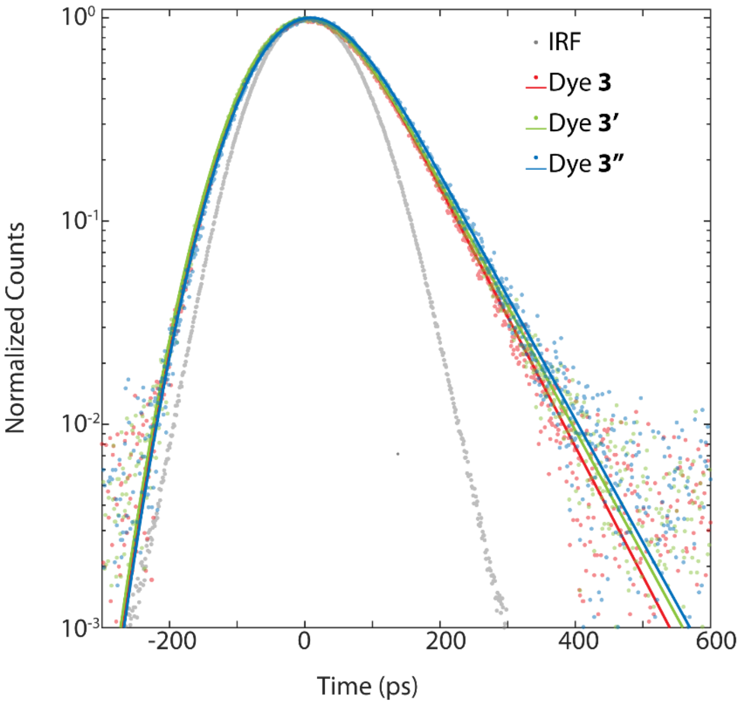

Figure S1: **Example lifetime fit:** Fitted lifetimes for dye **3**, **3'**,**3"**.

II. Modeling absorption and emission

This manuscript establishes the relationship between the energy gap and quantum yield of molecular systems in the shortwave infrared. In this supporting information, we will outline or derive the expressions that relate spectroscopic and structural observables to the radiative and non-radiative rates of a molecular chromophore, separating molecular details (e.g. transition dipole moment, number of/coupling to vibrations, and excited/ground state degeneracy) from photonic degrees of freedom (e.g. index of refraction and density of photon states as a function of energy gap).

a. Einstein coefficients, absorption, and emission. There is considerable ambiguity when describing how spectroscopic observables such as the molar absorptivity, lifetime and quantum yield relate to intrinsic molecular properties such as transition dipole moment and oscillator strength. Much of the literature defines these relationships in terms of gas-phase atomic transitions, and while the physics is identical for molecular systems, the presence of a stokes shift between absorption and emission, broader more complex lineshapes, a dielectric environment, and more complex excited state degeneracy complicates numerical comparison between chromophores.[8–12] Several papers clarify this discussion and we simply elaborate on their work below, keeping notation and unit consistency with our manuscript, and including solvent dielectric effect in all cases.[8–12] To guide the discussion, we provide a table of units for each of the terms given in both gaussian and SI unit systems (Table S1).

To relate the molar absorptivity to the rate of absorption (and ultimately the rate of emission), we will use the Einstein formalism, depicted in Figure S2. In steady state the change in population is zero ($N_1' = 0$), which allows us to express the following equation:

$$B_{12}^{E} N_1 u(E) = B_{21}^{E} N_2 u(E) + A_{21} N_2, \tag{S3}$$

Where B_{12}, B_{21} and A_{21} are the rate constants for absorption, stimulated emission and spontaneous emission respectively, $u(E)$ is the energy density of radiation per unit energy, and $N_1$and N_2 are the population of molecules in ψ_1 and ψ_2 respectively. The superscript omega denotes that these B coefficients include units of angular frequency as it is the rate of absorption or stimulated emission at a given excitation energy.

Table S1: Unit table

Variable	Gaussian (cgs)	SI units
$\boldsymbol{B_{12}\ or\ B_{21}}$	$\frac{cm}{g}$	$10\,\frac{m}{kg}$
$\boldsymbol{A_{21}}$	s^{-1}	s^{-1}
$\boldsymbol{I}$	$\frac{g}{s^2 cm}$	$10\,\frac{kg}{s^2 m}$
$\boldsymbol{\sigma_0}$	$cm^2 erg$	$10^{-3} m^2 J$
$\boldsymbol{\epsilon}$	$mol \cdot cm^2$	$10^4 mol \cdot m^2$
$\boldsymbol{u(E)(black\ body)}$	$\frac{g}{cm} erg$	$10^{-7}\,\frac{kg}{m} J$
$\boldsymbol{\langle U \rangle}$	$\frac{g}{s^2 \cdot cm}$	$0.1\,\frac{kg}{s^2 \cdot m}$
$\boldsymbol{\mu_{21}}$	D	$3.335 \times 10^{30} C \cdot m$

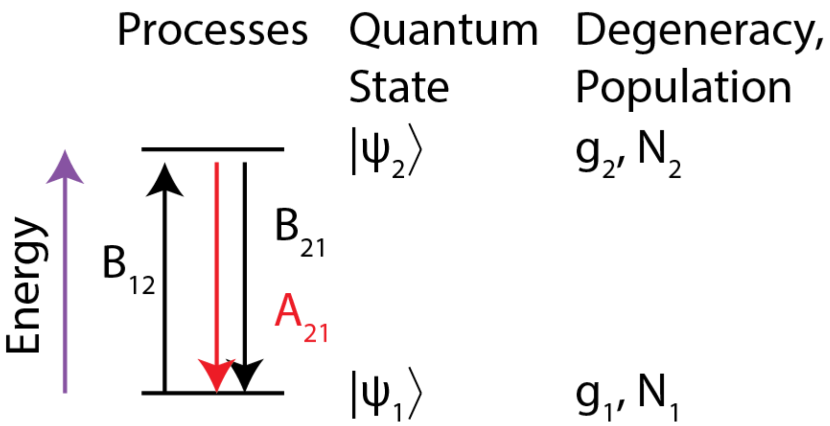

Figure S2: **Depiction of Einstein coefficients:** Defining induced absorption, stimulated emission, and spontaneous emission for a 2-level system

b. Absorption parameters to Einstein coefficients

The absorption cross section (*SI*: m^2) is measurable using a conventional UV-VIS spectrometer. The cross section is defined as the energy absorbed by the chromophore per unit time divided by the energy per unit area per unit time of incident light (*e.g.*, intensity). The energy absorbed per second is given by the rate of absorption, ($B_{12}^{E}u(E)$) (total units of s^{-1}), multiplied by the energy of each photon absorbed (E_g). The intensity is given by the average energy density of monochromatic light as $\langle U\rangle$ (energy per unit volume). The input intensity is therefore $I_0 = v\langle U\rangle$, where v is the speed of light in a dielectric medium, *i.e.* $v = c/n$. We arrive at the following expression for cross section:

$$\sigma(E) = \frac{nEB_{12}^{E}u(E)}{c\langle U\rangle} \tag{S4}$$

Which simplifies to

$$\sigma(E)dE = \frac{nEB_{12}^{E}}{c} \tag{S5}$$

where $\langle U\rangle = u(E)dE$. The change in intensity as a function of penetration depth of this incident light is

$$\frac{dI}{dx} = -N_1\sigma(E)I(x)dI \tag{S6}$$

which for a fixed path length, l, leads naturally to

$$\frac{I_{final}}{I_0} = e^{-N_1\sigma(E)l} \tag{S7}$$

A standard absorption spectrometer measures the intensity transmitted of absorbed light as a function of input frequency for a monochromatic beam. By chemistry convention the absorbance is

$$A(E) = -Log_{10}\frac{I(E)}{I_0(E)} = \epsilon(E)ML \tag{S8}$$

Where $\epsilon(E)$ is the molar absorptivity (or attenuation), M is the concentration of sample (commonly in units of molarity), and L is the path length. This translates to cross-section as follows.

$$\sigma(E) = \frac{1000}{N_A \log_{10} e}\epsilon(E) \approx 1.66 \times 10^{-21}\,\epsilon(E) \tag{S9}$$

In this paper, we will consider uniform illumination over the entire lowest energy absorption feature (usually well separated in the NIR or SWIR). Our coefficient therefore corresponds to the overall absorption of the lowest energy transition(s). We thus define single absorption coefficient σ_0 corresponding to the following integral

$$\sigma_0 = \int_{\omega_1}^{\omega_2} \sigma(E)dE \tag{S10}$$

We can also define a simple lineshape function $g(E) = \sigma(E)/\sigma_0$. This allows us to use either the overall Einstein coefficient B_{12}, or the coefficient at a specific wavelength $B_{12}^E = B_{12}g(E)$

To relate the measured total absorption cross section with emission, we will use the rest of the relevant Einstein coefficient relations. Without external illumination, (at thermal equilibrium) the population at each energy level is $\frac{N_2}{N_1} = \frac{g_2}{g_1}e^{-\beta E_g}$, where $\beta = (kT)^{-1}$, E_g is the energy gap, and g_1 and g_2 are the degeneracy of ground and excited state respectively. Here, we can use $u(\omega)$ the energy density of a blackbody at temperature T and v:

$$u(E) = \frac{E_g^3}{\pi^2 v^3 \hbar^2 (e^{\beta E} - 1)} \tag{S11}$$

Through substitution of N_2, $u(E)$, and v in S3 we arrive at

$$\frac{B_{12}E_g^3n^3}{\pi^2\hbar^2c^3} = \frac{g_2}{g_1}\frac{B_{21}E_g^3n^3}{\pi^2\hbar^2c^3}e^{-\beta E_g} + A_{21}\frac{g_2}{g_1}(1 - e^{-\beta E_g}) \tag{S12}$$

Equation S12 is true at all temperatures which allows us to relate absorption and spontaneous emission. For the low temperature limit (appropriate when $kT \ll \hbar\omega$), then $T \to 0, \beta \to \infty$

$$B_{12} = \frac{g_2}{g_1}\frac{\pi^2\hbar^2c^3}{E_g^3n^3} A_{21} \tag{S13}$$

Therefore, one can calculate the radiative rate from the absorption cross section, assuming we know the relevant energy gap (E_g) and the ratio of the degeneracy between ground and excited states.

$$\sigma_0 = \frac{n\hbar E_g B_{12}}{c} = \frac{g_2}{g_1}\frac{A_{21}\pi^2\hbar^3c^2}{E_g^2n^2} \tag{S14}$$

We obtain A_{21}independently by measuring the lifetime and quantum yield of each dye (see Section I), we can compare each to determine the degeneracy ratio $\frac{g_2}{g_1}$ for each dye.

In this paper, to compare absorption and emission measurements we assume a common energy gap for all photophysical measurements, in this case the midpoint between absorption and emission. Within the displaced harmonic oscillator model, E_g is the energy difference between harmonic wells. As cyanine dyes have small stokes shifts and low Huang Rhys factors, we believe this simplification will introduce minimal relative errors. We can therefore relate our absorption cross section to the spontaneous (radiative) rate.

$$A_{21} = \frac{g_1}{g_2}\frac{E_g^2n^2}{\hbar^3\pi^2c^2}\ \sigma_0 = \frac{g_1}{g_2}\frac{1000E_g^2n^2}{N_a Log_{10}(e)\pi^2\hbar^3c^2}\int_{E_1}^{E_2}\epsilon(E)dE \tag{S15}$$

c. Comparison to the Strickler-Berg equation

The spontaneous radiative rate coefficient derived here matches that derived by Strickler and Berg with appropriate unit conversions (reproduced below in both the common condensed form and its expanded form).[9]

$$\begin{aligned} A_{21} &= 2.88 \times 10^{-9} n^2 \langle \tilde{v}_f^{-3} \rangle^{-1} \frac{g_1}{g_2}\int_{\omega_1}^{\omega_2} \epsilon(\tilde{v}) d\ln(\tilde{v}) \\ &= \frac{8 \times 1000\pi c n^2}{N_A \log_{10} e} n^2 \langle \tilde{v}_f^{-3} \rangle^{-1} \frac{g_1}{g_2}\int_{\omega_1}^{\omega_2} \epsilon(\tilde{v}) d\ln(\tilde{v}) \end{aligned} \tag{S16}$$

Note that this equation, energy is defined in wavenumber not energy defined in Joules as described above. Additionally, The Strickler-Berg accounts for the molecular band gap differently by differentiating between the emission energy and the absorption energy such that the carrier frequency is defined by the fluorescence spectra. While this is a reasonable approximation, it renders absorption and emission metrics of radiative rates internally inconsistent, so we will use the mid-gap point instead.

d. Relating Einstein coefficients to transition dipole moments

The transition dipole moment is the molecular parameter which sets the strength of absorption and the rate of emission for dipole allowed transitions. We can derive the relationship between the transition dipole moment and radiative rate through an application of Fermi's Golden rule. The transition rate comes from first order perturbation theory.[13]

$$A_{21} = \frac{2\pi}{\hbar}|M_{21}|^2 g(E_g) \tag{S17}$$

In free space, $g(E_g)$, can be computed by computing the number of photon modes in a cavity of volume V_0.

$$g(E_g) = \frac{E_g^2 V_0}{\pi^2 \hbar^2 v^3} \tag{S18}$$

For a randomly oriented dipole in free space the transition matrix is

$$|M_{12}|^2 = \frac{1}{3}\mu_{21}^2 \mathcal{E}_{vac}^2 \tag{S19}$$

With the magnitude of energy of the fluctuating electric field in a vacuum defined as.

$$\varepsilon_{vac} = \left(\frac{E_g}{2\varepsilon_0 V_0}\right)^{\frac{1}{2}} \tag{S20}$$

Combining Equations S17-20.

$$A_{21} = \frac{\mu_{21}^2 E_g^3}{3\pi \hbar^4 v^3 \varepsilon} \tag{S21}$$

We modify this slightly by including the refractive index $\varepsilon = \varepsilon_0 n^2$ (in cgs units $\varepsilon = \frac{1}{4\pi} n^2$). With this correction, we arrive at

$$A_{21} = \frac{4\mu_{21}^2 E_g^3 n}{3\hbar^4 c^3} \tag{S22}$$

Which is identical to the equation found in the prior literature with the addition of the refractive index correction.[8] We can therefore relate transition dipole moment to the absorption cross section using S14 and S22 as follows:

$$\mu_{21}^2 = \frac{g_1}{g_2}\frac{3\hbar n c}{4E_g \pi^2}\,\sigma_0 \tag{S23}$$

e. Oscillator strength

Oscillator strength is defined as the comparison of the absorption or emission rate to the rate of absorption or emission of a classical oscillator. The classical oscillator rate of transition is defined as

$$\gamma_{cl} = \frac{q^2 E_g^2 n}{6\pi \varepsilon_O m \hbar^2 c^3} \tag{S24}$$

where m is the mass of an electron and q is electron charge. We then can define the emission oscillator strength as

$$f_{21} = -\frac{\frac{1}{3}A_{21}}{\gamma_{cl}}. \tag{S25}$$

We use the radiative rate found through use of quantum yield and total lifetime to determine the oscillator strength of emission. Similar to how B_{12} and B_{21} are related by the degeneracy ratio so are f_{12} and f_{21}. We can solve for f_{12} with the relationship between the classical oscillator cross section, σ_{oc}, compared to the experimental absorption cross section.[8]

$$\sigma_{oc} = \int_{-\infty}^{\infty} \frac{\frac{\gamma_{cl}}{2\pi}}{\left(\frac{E}{\hbar} - \frac{E_0}{\hbar}\right)^2 + \left(\frac{\gamma_{cl}}{2}\right)^2} \frac{\pi q^2}{2\varepsilon_0 mc} dE \tag{S26}$$

$$f_{12} = \sigma_0/\sigma_{0c} \Rightarrow \frac{2\varepsilon mc}{\pi\hbar q^2} \sigma_0 \tag{S27}$$

III. Nonradiative rate estimation

a. Exponential rate law assumptions.

We summarize the nonradiative rate energy gap law as derived in Englman and Jortner (E&J) and shown in Equation 5. E&J notes that internal conversion in large molecules closely resembles the mutiphonon relaxation in semiconductors. In short, the large number of vibrational frequencies resembles a quasicontinuum of transitions which can weakly couple the ground and excited states. They then derive the rate equations in two limits, the first applicable for systems with large stokes shifts relative to the energy gaps (appropriate for systems with avoided crossing or conical intersections), and the other applicable with small stokes shifts relative to the energy gap (relevant to our work). Within the latter limit, it is possible to evaluate the rate as defined below for first order perturbation theory (or Fermi's Golden Rule). Therefore, the rate is as follows

$$W = \frac{2\pi}{\hbar}\sum_{i}\sum_{j} p(si)\left|V_{si,lj}\right|^{2}\delta(E_{si} - E_{lj}) \tag{S28}$$

Where $p(si)$is the occupation of a given mode on the excited state. They further simplify this equation to

$$V_{si,lj} \approx CS_{si,lj} \tag{S29}$$

Where C is the coupling term between ground and excited states, and $S_{si,lj}$ are the Franck Condon overlap factors.

$$S_{si,lj} = \prod_{t}\left\langle X_{e,t}\left(Q_{t}^{(e)}, \nu_{e,t}\right)\middle| X_{gt}\left(Q_{t}^{(g)}, \nu_{g,t}\right)\right\rangle \tag{S30}$$

Where $X_{(e,g)t}\left(Q_{t}^{(e,g)}, \nu_{(e,g),t}\right)$ are the excited or ground nuclear wavefunctions.

C is derived in a previous paper,[14] and is the total derivative or Hertzberg-Teller coupling,[15,16] the largest perturbation to the Born-Oppenheimer approximation which couples ground and excited states. While this is challenging to calculate or experimentally determine, estimates typically range from $10^{2}\ \mathrm{cm}^{-1}$ to $10^{4}\ \mathrm{cm}^{-1}$, for which we use $2000\ \mathrm{cm}^{-1}$ and $4080\ \mathrm{cm}^{-1}$ in our manuscript.

E&J arrive at a method for evaluating the Franck-Condon overlap factors through the use of the displaced harmonic oscillator model combined with a generating function method.[17] Within the weak coupling limit (where the stokes shift is small) they evaluate the summation using the method of steepest descent, arriving at the expression shown in Equation 6. Within this estimate, they find that the highest energy vibration contributes the most to the summed overlap integral, which for organic molecules is typically the C-H stretch.

To allow for clarity between E&J equation and the version used in the text in order to simplify and allow for it to be combined with radiative rate expressions.

E&J denotes the equation as

$$k_{nr} = \frac{C^{2}\sqrt{2\pi}}{\hbar\sqrt{\hbar\omega_{M}\Delta E}}\exp\left[-\frac{\Delta E}{\hbar\omega_{M}}\left(\ln\left(\frac{2\Delta E}{d\hbar\omega_{M}\Delta_{M}^{2}}\right) - 1\right)\right]. \tag{S31}$$

Where, ΔE is the energy at the HOMO-LUMO gap, ω_{M} is the maximum vibration, d is the number of degenerate or near degenerate modes, Δ_{M} is the reduced displacement of the maximum transition. $\hbar\omega_{M}$ and ΔE are changed to E_{M} and E_{g}, respectively. The main changes are made to the $d\hbar\omega_{M}\Delta_{M}^{2}$ terms, as these relate to parameters to more spectroscopic variables.

We can relate these vibrational displacement parameters to the stokes shift, E_{ST}, as a summation of all the vibrations coupled to the electronic transition.

$$E_{ST} = \sum_{j}\hbar\omega_{j}\Delta_{j}^{2} \geq d\hbar\omega_{M}\Delta_{M}^{2} \tag{S32}$$

We can thus recast the $d\hbar\omega_{M}\Delta_{M}^{2}$ as a proportion of the total stokes shift, γ_{M}, such that $\gamma_{M} = \frac{d\hbar\omega_{M}\Delta_{M}^{2}}{E_{ST}}$. Plugging into Equation S31 , we get the equation in the text.

$$k_{nr} = \frac{C^2\sqrt{2\pi}}{\hbar\sqrt{\hbar\omega_M E_g}} \exp\left[-\frac{\Delta E}{\hbar\omega_M}\left(\ln\left(\frac{2E_g}{\gamma_M E_{ST}}\right) - 1\right)\right]. \tag{S33}$$

We also test tested if the Huang Rhys parameter of 0.1 for a C-H mode would be observable. Based on a simple Frank Condon model, we see that under the ideal pessimistic scenario this peak could be resolved though the intensity is considerably under the background (Figure S3). Our results suggest that a 0.1 H-R coupled 3000 cm^{-1} vibronic feature is plausible under the absorption envelope.

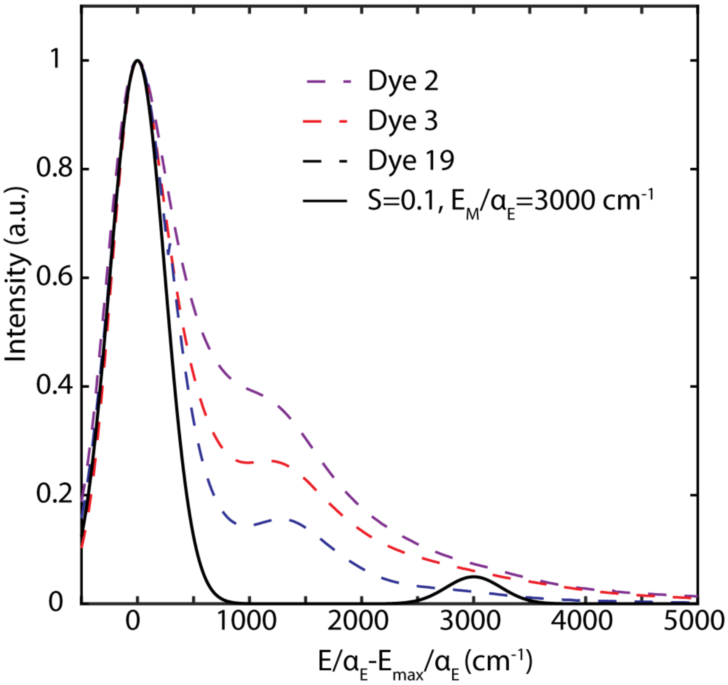

Figure S3: **Vibronic feature comparison:** Comparison of a 3000 cm^{-1} vibronic feature with an S=0.1 to a selection of dyes that are centered to their maximum peak energy.

b. Impact of γ_m and C on quantum yield

In Figure S4, we test the how variance in γ_M and C affect the quantum yield fit (Equation 8). Decreasing both parameters, shifts the energy at which the quantum yield precipitously falls off further into the red as both parameters impact the amount of coupling to the vibrational relaxation manifold.

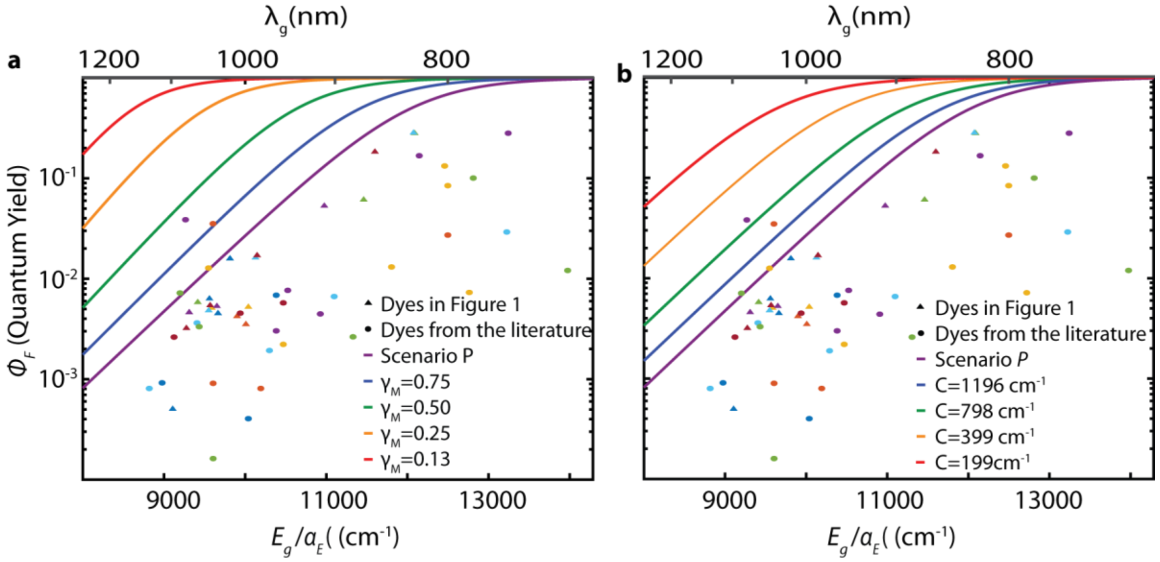

Figure S4: **Impact of γ_M or C on the quantum yield with respect to energy gap.** Plots showing the impact of changing a) The degree to which the high frequency mode couples to the quantum yield (γ_m) and b) The nonadiabatic coupling (C) on the quantum yield while keeping the other value held constant. Scenario P represents the pessimistic case.

IV. EQME with labelled polymethine dyes

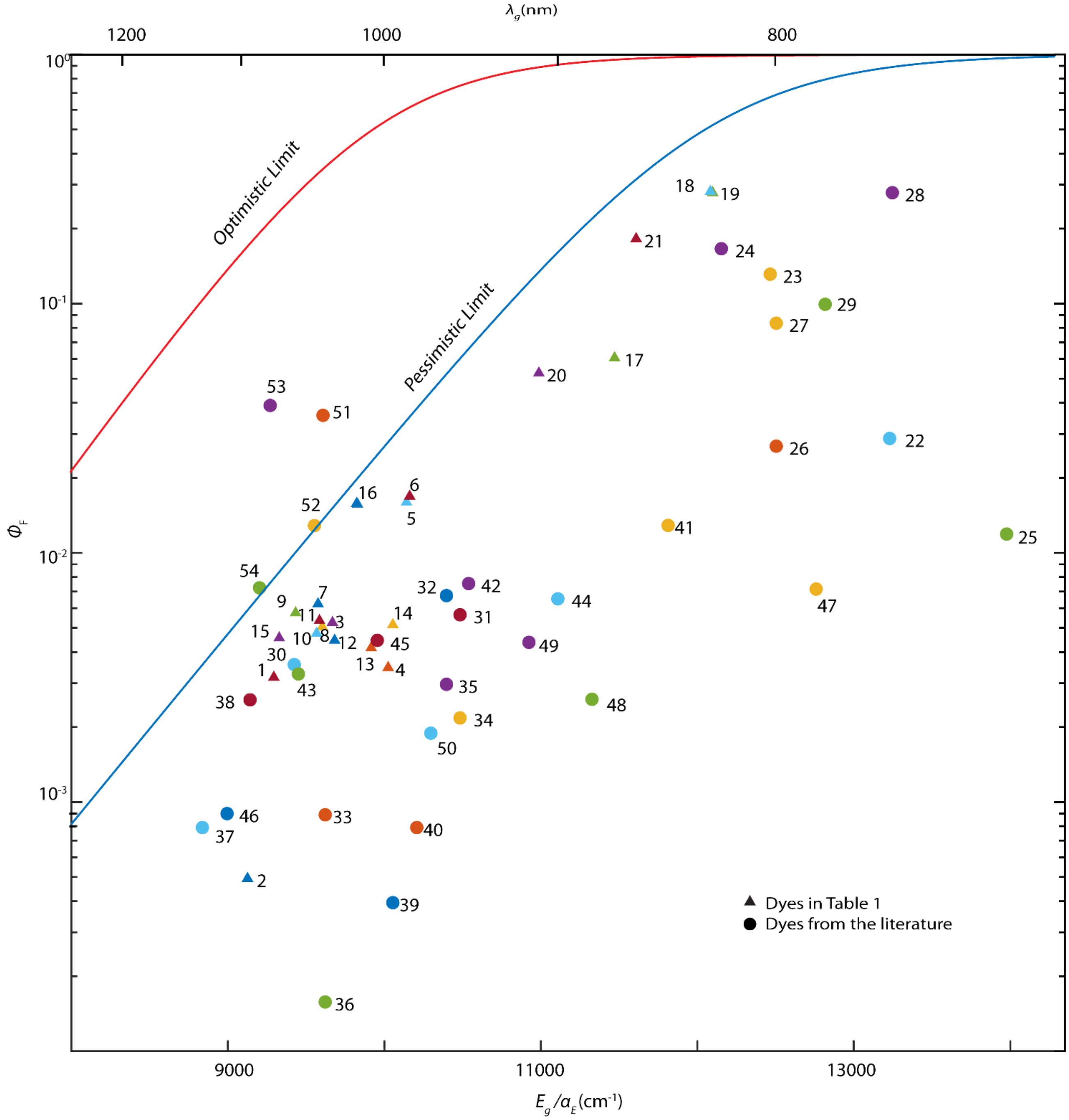

Figure S5: **Labelled Version of Figure 5.** Combined Energy Gap Law for optimistic and pessimistic cases, with a key for the points in Table S2.

Table S2: Key for Figure S5

Label	Dye	**Label**	Dye	**Label**	Dye
1	IR-1061[3]	**19**	8[2]	**37**	5L5 in DCE[18]
2	IR-26[1]	**20**	4[2]	**38**	5H5 in DCE[18]
3	1(Flav 7) [1]	**21**	10[2]	**39**	6L6 in DCE[18]
4	11(IR-27) [1]	**22**	Flav3[3]	**40**	6H6 in DCE[18]
5	7[2]	**23**	IR-125[19]	**41**	Rh824[20]
6	5[2]	**24**	IR-140[19]	**42**	Rh923[20]
7	2[1]	**25**	Cryptocyanine[19]	**43**	Rh1093[20]
8	4[1]	**26**	ICG in PBS[21]	**44**	CX1 in $CHCl_3$[22]
9	7[1]	**27**	ICG in 70:30 EtOH:H_2O[21]	**45**	CX2 in $CHCl_3$[22]
10	5[1]	**28**	HITC[21]	**46**	CX3 in $CHCl_3$[22]
11	6[1]	**29**	IR-800[23]	**47**	8[7]
12	8[1]	**30**	FD-1080 in EtOH[24]	**48**	7[7]
13	9[1]	**31**	BTC980 in DCE[25]	**49**	10[7]
14	10[1]	**32**	BTC982 in DCE[25]	**50**	11[7]
15	3(JuloFlav7)[1]	**33**	BTC1070 in DCE[25]	**51**	LZ-1060 in CH_3OH[26]
16	9[2]	**34**	BTC980 in PBS[25]	**52**	LZ-1092 in CH_3OH[26]
17	2[2]	**35**	BTC982 in PBS[25]	**53**	LZ-1105 in CH_3OH[26]
18	6[2]	**36**	BTC1070 in PBS[25]	**54**	LZ-1118 in CH_3OH[26]

V. Derivation of comparison equation

We desire a method to compare chromophores with different energy gaps. We observe that the log of the quantum yield varies linearly in the NIR and SWIR for our parameters. Therefore, we will use a linear model to develop an energy-gap independent quantum yield comparator.

We will assume that we have two chromophores, a and b with quantum yields ϕ_a and ϕ_b, and energy gaps E_a and E_b. Here, we define $\phi_a^\dagger$ as the prediction of what the quantum yield of a would be at E_b. We define improvement factor as $\zeta = \frac{\phi_b - \phi_a^\dagger}{\phi_a^\dagger}$. Values greater than zero indicate improvement relative to the energy gap law expectation. We can predict $\phi_a^\dagger$

is the quantum yield prediction of chromophore *b* given the molecular properties from chromophore *a* and the linear approximation of this energy gap law such that:

$$\ln\left(\phi_a^\dagger\right) = \kappa(\Delta E) + \ln(\phi_a) \tag{S34}$$

$$\phi_a^\dagger = \phi_a e^{\kappa \Delta E} \tag{S35}$$

Where $\Delta E = E_b - E_a$.

Plugging back into our improvement factor we have the improvement factor as defined in the main text.

$$\frac{\phi_b}{\phi_a} e^{-\kappa \Delta E} - 1 \tag{S36}$$

The slope κ can be found from taking the natural log of Equation 8 leading to the following expression

$$\ln \phi\left(E_g\right) = \ln\left(1 + \frac{3\epsilon_0 c^2 C^2}{2^{\frac{5}{2}} \pi^{\frac{3}{2}} \mu_{12}^2 n E_M^{\frac{1}{2}} E_g^{\frac{7}{2}}} \exp\left[-\frac{E_g}{E_M}\left(\ln \frac{2E_g}{\gamma_M E_{ST}} - 1\right)\right]\right)^{-1}. \tag{S37}$$

Combining constants, we arrive at:

$$\ln \phi\left(E_g\right) = \ln\left(1 + aE_g^{-\frac{7}{2}} \exp\left[-bE_g\left(\ln\left(\mathrm{cE_g}\right) - 1\right)\right]\right)^{-1}. \tag{S38}$$

If the second term in S35 is larger than 1, (true for low QY samples), we consider the following equation which we will take the derivative of to find the slope.

$$\frac{\mathrm{d}\ln \phi\left(E_g\right)}{\mathrm{dE_g}} = \frac{\mathrm{d}}{\mathrm{dE_g}}\left(-\ln\left(aE_g^{-\frac{7}{2}} \exp\left[-bE_g\left(\ln(\mathrm{cE_g}) - 1\right)\right]\right)\right) \tag{S39}$$

$$\frac{\mathrm{d}\ln \phi\left(E_g\right)}{\mathrm{dE_g}} = \frac{7}{2E_g} + b(\ln\left(cE_g\right) \tag{S40}$$

Assuming that $\gamma_M = 1$ we arrive at the following expression.

$$\frac{\mathrm{d}\ln \phi\left(E_g\right)}{\mathrm{dE_g}} = \kappa = \frac{7}{2E_g} + \frac{1}{E_M}(\ln\left(\frac{2E_g}{\gamma_M E_{ST}}\right) \tag{S38}$$

We show that κ slightly overestimates the numerically evaluated slope in Figure S6 from 950 to 1200 nm This indicates that our numbers evaluate a conservative estimate of improvement

a. Enhanced worked example:

In Figure S7 we compare dyes **2**–**4** (common names, IR-26, Flav7, and IR-27, respectively). While all of the dyes have identical methine bridges, they differ in their heterocycle, which leads to large changes in quantum yield and absorption energy. For simplicity, we chose dye **2** to be chromophore *a*. When we plug in $\frac{E_{g,a}}{\alpha_E} = 9107\ \mathrm{cm}^{-1}, \gamma_M = 1, \frac{E_{ST}}{\alpha_E} = 298.7\ \mathrm{cm}^{-1} and\, \frac{E_M}{\alpha_E} = 3000\ \mathrm{cm}^{-1}$ into equation 11 or S38 and reproduced below $, \kappa\alpha_E\ \ 0.0014$ cm, for this analysis.

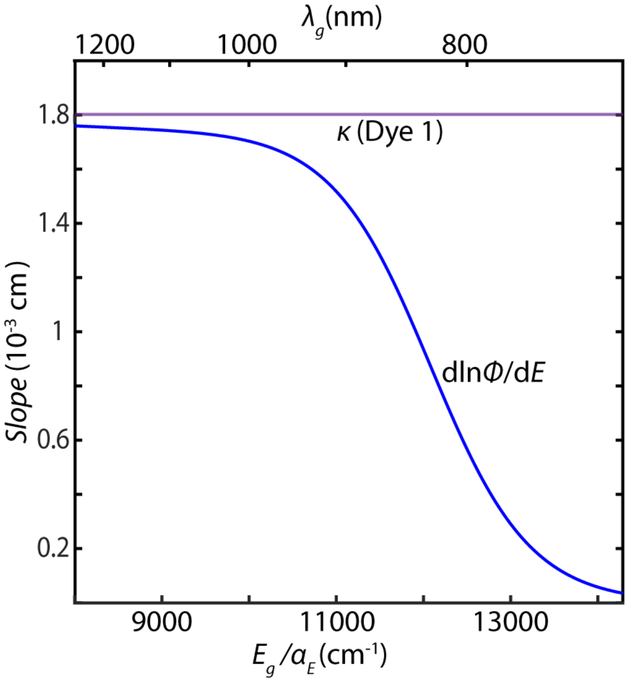

Figure S6: **EQME slope versus the κ estimate:** Comparison of the slope estimation described above to a numerical derivative of the natural log of the slope and the inverse of the nonradiative rate.

IR-26 is the reddest chromophore in our dataset ($\lambda_{max} = 1080\,, \phi_F = 5 \times 10^{-4}$), while IR-27 substitutes the oxygen for sulfur in the heterocycle, resulting in a $93\ \mathrm{nm}$ blueshift and an increase in quantum yield $\phi_F = 3.2 \times 10^{-3}$. Previously, we hypothesized that the improvement in quantum yield arises from a decreased heavy atom effect, leading to lower intersystem crossing rates.[3] However, to fully assess this claim we need to deconvolute the effect of the change in E_g in resultant ϕ_F. Using values defined above and $\frac{E_{g,b}}{\alpha_E} = 100011\ \mathrm{cm}^{-1}$ into Equation 10 or S36 We find that the energy gap independent improvement factor for IR-26 to IR-27 of $\xi = 0.9$, i.e. IR-27 is 1.9 times ($\xi + 1$) more emissive, even when adjusted for its blue-shifted energy gap, still an improvement, but considerably less impressive than the apparent $\chi = 6$ improvement factor. Flav7 adds an additional dimethyl amino group and replaces sulfur in the IR-26 scaffold. These structural changes both increase the quantum yield to $6.1 \times 10^{-3}$and blue shift the chromophore 53 nm, leading to a direct improvement of $\chi = 11.2$ in ϕ_F relative to IR-26. However, the adjusted improvement is only $\xi = 4.6$.

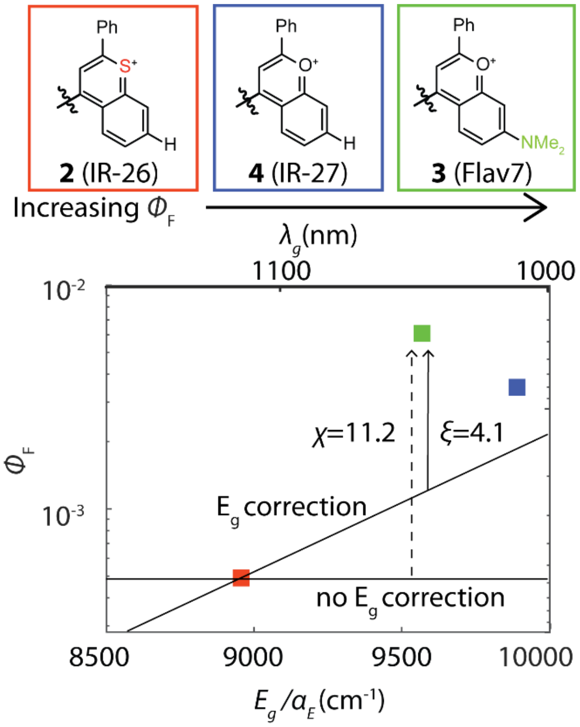

Figure S7: **Worked out Example of the energy gap independent parameter.** IR-26, IR-27 and Flav7 show increasing quantum yields. To compare these dyes, we apply an energy gap independent comparator, ξ, which factors in the change in E_g.

b. Comparison relative to IR-27 (dye 4)

We compared all the dyes with an energy gap above 950 nm (7-methine family) in the main text to Dye **4** (Figure S8 and Table 3). These results confirm that the energy gap dependence can account for significant improvements in QY. We note that scaffolds that remove alkenyl C-H stretches compared to Dye **3**, especially removal of the 2-position phenyl group (**5**, **6**), seem to improve even with energy gap.

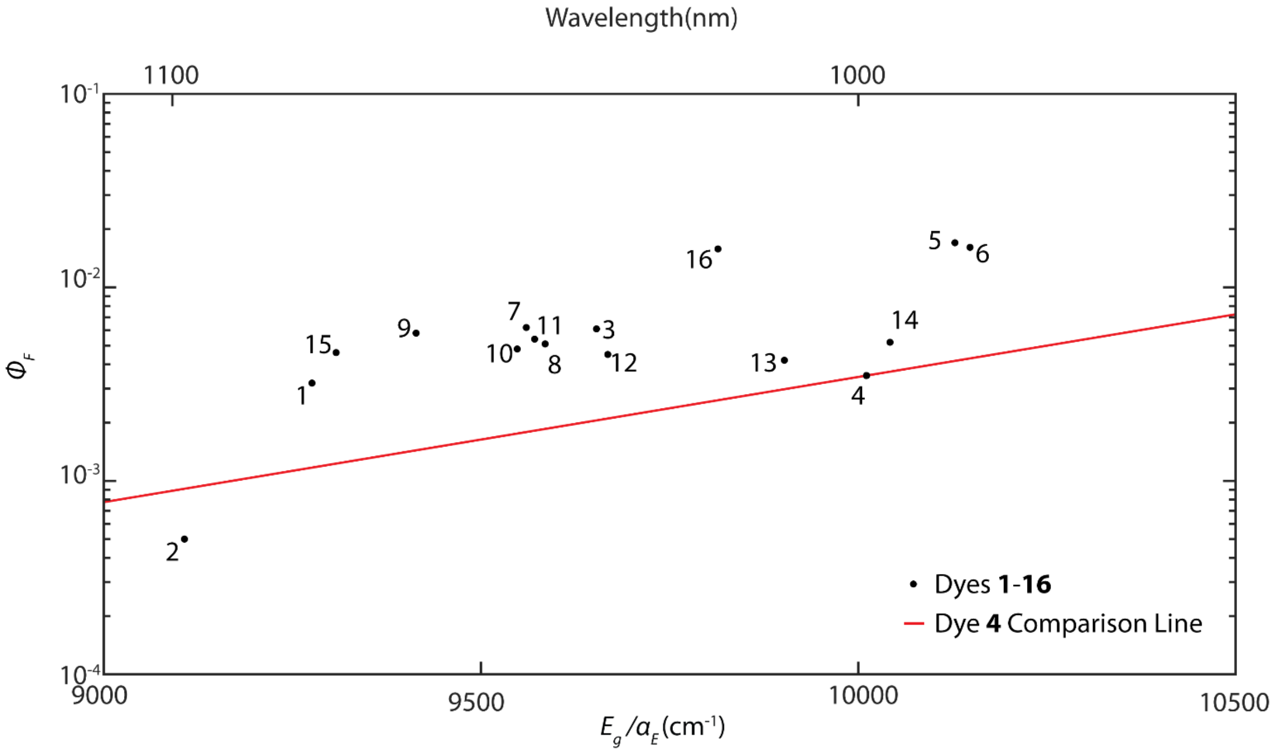

Figure S8: **Energy gap independent parameter using Dye 4 as the standard:** Simplified energy gap law assuming that dye **4** is the point of comparison for the 16 dyes analyzed in the manuscript table with values below.

VI. Overcoming energy gap laws

a. Enhancement from changing maximum vibrational stretch comparing parameters

We show how our methods of improvement changed depending on our pessimistic (scenario *P*) compared to our optimistic (scenario *O*) parameter. Given that only changing the maximum energy vibronic stretch impacted the location of maximum enhancement that is produced in Figure S6. Decreasing γ_m and C compared to scenario *P* both red shifted our peak enhancement to the red as well as decreasing the amount of enhancement (Figure S9). For the change in transition dipole, we see a similar trend, where the onset of the increase in enhancement is redshifted. Thus, experimental verification of γ_m and C is necessary to fully understand the full impact of changing the maximum vibrational character on quantum yield

b. Synthesis and characterization of dye 3' and 3"

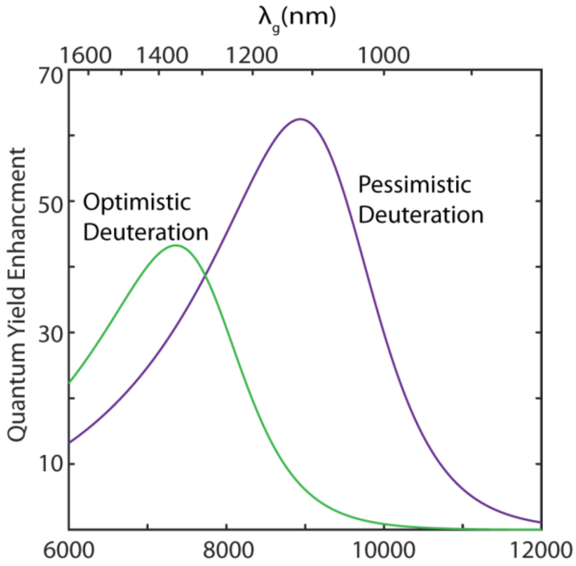

Figure S9: **Impact of Deuteration based on different EQME conditions:** Enhancement by switching all $\mathrm{E_{vib}}$ from C-H stretch to C-D stretch for scenario O and P.

<u>General synthetic procedures</u>

Chemical reagents were purchased from Sigma-Aldrich (cyclohexanone, acetyl chloride and phosphoryl chloride), Fisher Scientific (solvents, sodium acetate and acetic anhydride), TCI America (aniline), and Cambridge Isotope Laboratory (deuterated compounds). 7-(Dimethylamino)-4-methyl-2-phenylchromenylium tetrafluoroborate (**S2**) was synthesized according to published procedure.[1] THF was dispensed from a Grubb's-type Phoenix Solvent Drying System constructed by JC Meyer. Nuclear magnetic resonance (^{1}H NMR, ^{13}C NMR) spectra were taken on a Bruker DRX500 or AV500 spectrometer. All chemical shifts in ^{1}H NMR and ^{13}C NMR are reported in the standard notation of ppm relative to residual solvent peak (DMSO-d_6 H=2.50, C=39.52). High resolution mass spectrometry was acquired on a Thermo Scientific Q Exactive Plus Hybrid Quadrupole-Orbitrap M with Dionex UltiMate 3000 RSLCnano System. Absorption spectra were collected on a JASCO V-770 UV–visible/NIR spectrophotometer after blanking with the appropriate solvent. Photoluminescence spectra were obtained on a Horiba Instruments PTI QuantaMaster Series fluorometer equipped with InGaAs detector. Samples were dissolved in HPLC grade CH_2Cl_2 and measured in Quartz cuvettes (2 mm × 10 mm) for absorption and photoluminescence measurements. All spectra were obtained at ambient temperature.

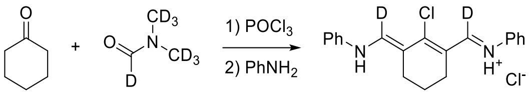

S1

***N*-((2-chloro-3-((phenylimino)methyl-*d*)cyclohex-2-en-1-ylidene)methyl-*d*)aniline hydrochloride salt** (**S1**): *N*,*N*-Dimethylformamide-d_7 (1.00 g, 12.5 mmol, 2.5 equiv.) was cooled in ice bath and phospohryl chloride (1.0 mL, 11 mmol, 2.2 equiv.) was added dropwise. The mixture was stirred for 0.5 h to form a white, thick suspension. To this mixture was added cyclohexanone (0.52 mL, 5.0 mmol, 1.0 equiv.) and the mixture was heated at 90 °C for 1 h. After cooling to room temperature, aniline (0.91 mL, 9.9 mmol, 2.0 equiv.) was added and further stirred for 1 h. The dark red mixture was transferred into a separatory funnel, diluted with H_2O (50 mL) and neutralized with $NaHCO_3$. The aqueous phase was extracted with CH_2Cl_2 (3 × 50 mL). The combined organic layer was dried (Na_2SO_4), concentrated and purified by column chromatography (1:10 ethyl acetate / hexanes). Collected yellow fractions were acidified by dry HCl in MeOH prepared by dissolving acetyl chloride (0.36 mL, 10 mmol, 2.0 equiv.) in MeOH (5 mL), concentrated to dryness and further washed with diethyl ether to afford **S1** as a dark red solid (454 mg, 1.26 mmol, 25%). R_f = 0.7 in 1:2 ethyl acetate/hexanes. ^{1}H NMR (500 MHz, DMSO-d_6) δ 11.61 (s, 2H), 7.64 (d, *J* = 8.4 Hz, 4H), 7.44 (q, *J* = 7.3 Hz, 4H), 7.25 (t, *J* = 7.4 Hz, 2H), 2.77 (t, *J* = 6.0 Hz, 4H), 1.87–1.78 (m, 2H). ^{13}C NMR (126 MHz, DMSO-d_6) δ 139.6, 129.7, 126.2, 119.0, 114.9, 48.6, 24.9, 19.5. HRMS (ESI$^+$) m/z calcd for $C_{20}H_{18}D_2ClN_2^+$ [M+H$^+$]: 325.1435, found 325.1433

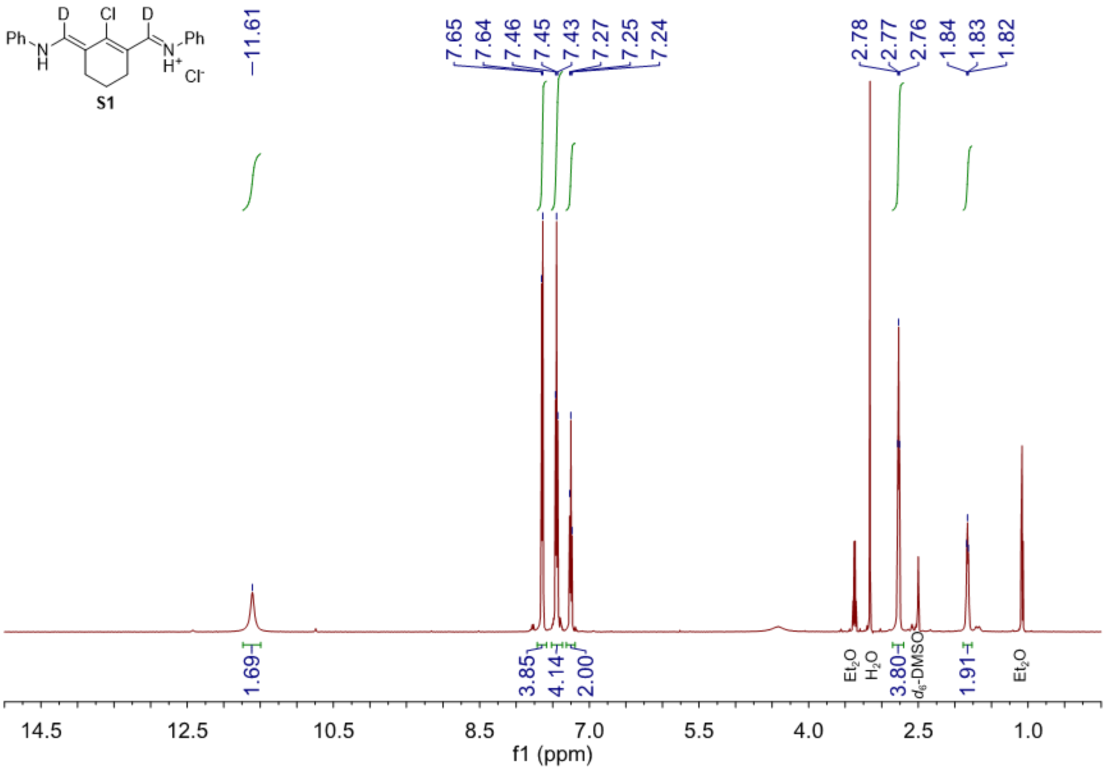
Ph
N
H
D
Cl
D
N
Ph
H+
Cl-
S1
11.61
7.65
7.64
7.46
7.45
7.43
7.27
7.25
7.24
2.78
2.77
2.76
1.84
1.83
1.82
1.69
3.85
4.14
2.00
Et2O
H2O
3.80
d6-DMSO
1.91
Et2O
14.5
12.5
10.5
8.5
7.0
5.5
4.0
2.5
1.0
f1 (ppm)

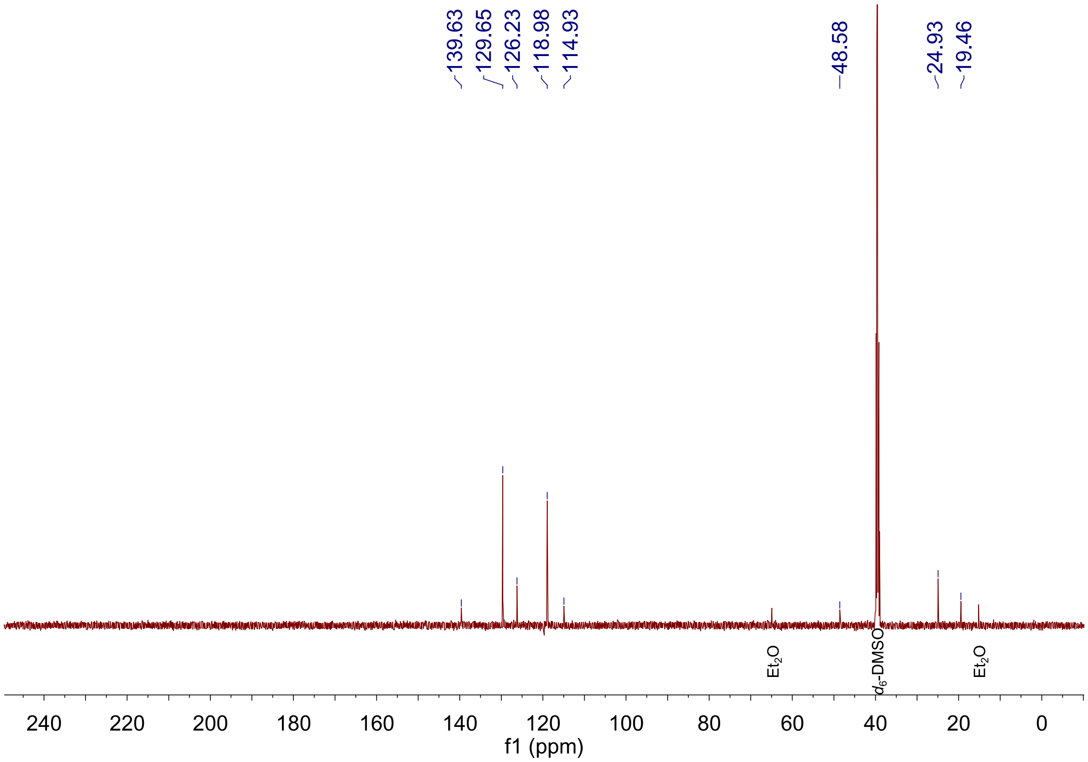
139.63
129.65
126.23
118.98
114.93
48.58
24.93
19.46
Et2O
d6-DMSO
Et2O
240
220
200
180
160
140
120
100
80
60
40
20
0
f1 (ppm)

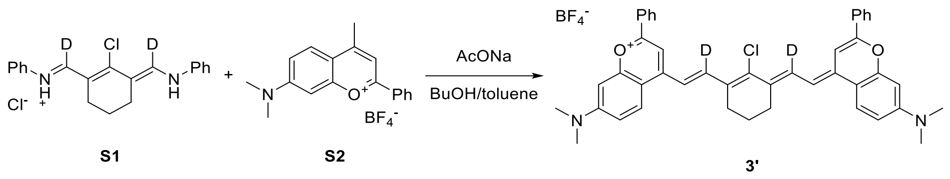

4-(2-(2-Chloro-3-(2-(7-(dimethylamino)-2-phenyl-4H-chromen-4-ylidene)ethylidene)cyclohex-1-en-1-yl)vinyl)-7-(dimethylamino)-2-phenylchromenylium tetrafluoroborate-*d*$_2$ (3'): To a 4 mL vial containing **S1** (31 mg, 0.085 mmol, 0.45 equiv.), **S2** (66 mg, 0.19 mmol, 1.0 equiv.) and sodium acetate (46 mg, 0.56 mmol, 3 equiv.) was added 3:7 butanol / toluene (2 mL) followed by immediate freeze-pump-thaw × 3. The mixture was stirred at 100 °C under N_2, cooled and concentrated to dryness. The dark mixture was separated by column chromatography (1:50 EtOH/CH_2Cl_2) to give **3'** as a dark purple solid (17 mg, 0.022 mmol, 27%). ^{1}H NMR (500 MHz, DMSO) δ 7.99 (s, 6H), 7.61 – 7.50 (m, 6H), 7.45 (s, 2H), 6.90 (s, 2H), 6.85 (d, *J* = 9.0 Hz, 2H), 6.65 (s, 2H), 3.08 (s, 12H), 2.76 (s, 4H), 1.88 (s, 2H). Absorbance (CH_2Cl_2): 523, 917, 1027 nm. Absorption coefficient $\varepsilon_{max} = (2.3\ \pm\ 0.1) \times 10^5\ \mathrm{M^{-1}cm^{-1}}$= (n = 2, average ± range) Emission (CH_2Cl_2, ex. 900 nm): 1053 nm. HRMS (ESI$^+$) m/z calcd for $C_{44}H_{38}D_2ClN_2O_2^+$ [M$^+$]: 665.2898, found 665.2907.

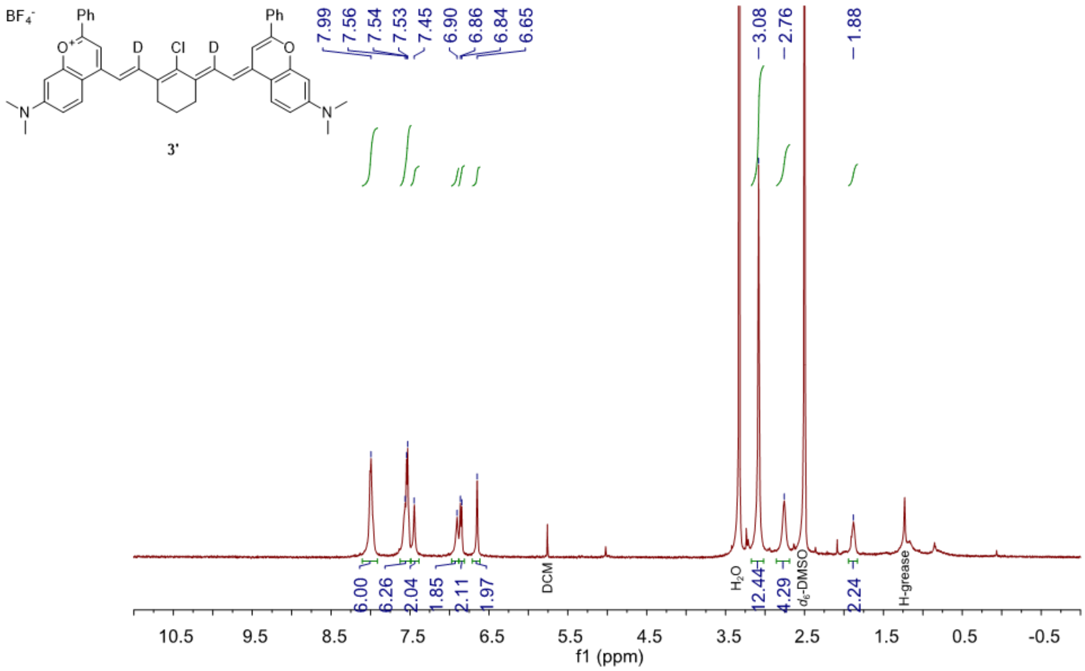

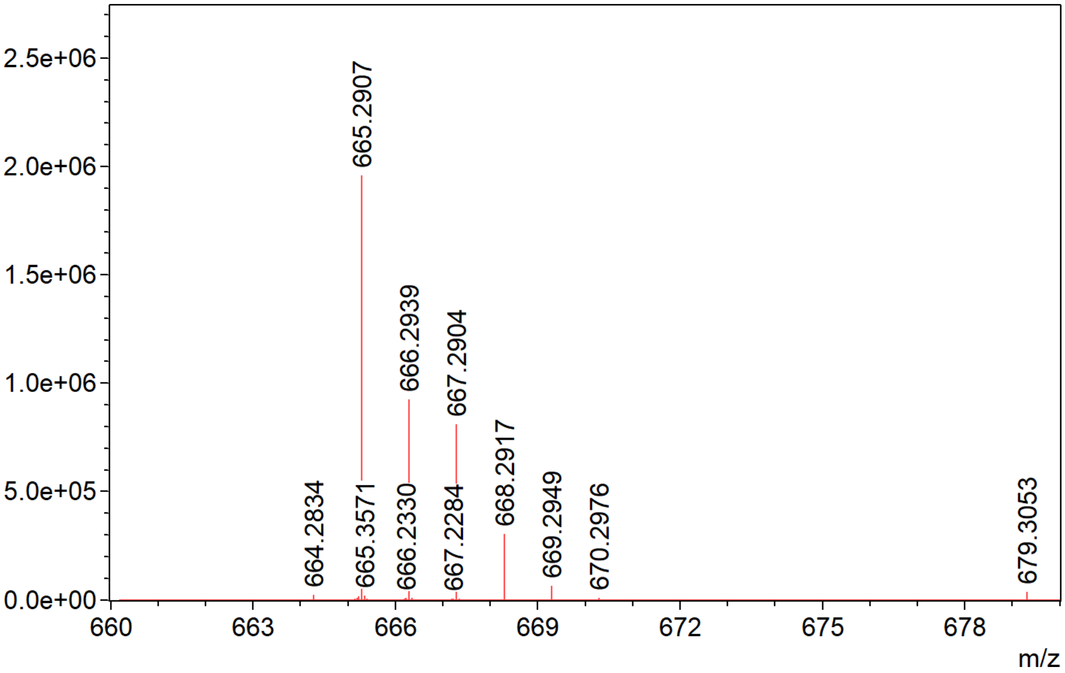

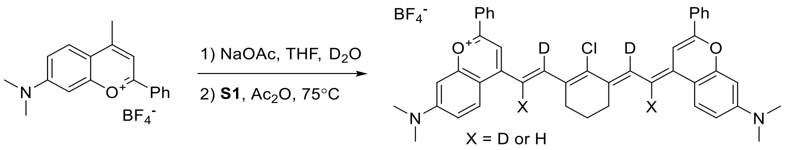

S2

3"

4-(2-(2-Chloro-3-(2-(7-(dimethylamino)-2-phenyl-4H-chromen-4-ylidene)ethylidene)cyclohex-1-en-1-yl)vinyl)-7-(dimethylamino)-2-phenylchromenylium tetrafluoroborate-*d*$_{2\text{-}4}$ (**3"**): **S2** (50 mg, 0.14 mmol, 1.0 equiv.) and sodium acetate (35 mg, 0.43 mmol, 3.0 equiv.) were dissolved in D$_2$O (1.3 mL) and dry THF (1.3 mL) followed by immediate freeze-pump-thaw × 3. The mixture was heated at 40 °C under N$_2$ for 4 h. The solvent was then lyophilized and this procedure was repeated to maximize deuterium exchange. At this point, mass spectra suggest >80% methyl hydrogen atoms were exchanged to deuterium atoms. To the dried mixture was added **S1** (23 mg, 0.064 mmol, 0.45 equiv.) and acetic anhydride (3 mL) followed by immediate freeze-pump-thaw × 3. The mixture was stirred at 75 °C under N$_2$ for 15 min, cooled and concentrated to dryness. The dark mixture was washed with toluene and separated by column chromatography (1:75 EtOH/CH$_2$Cl$_2$) to give **3"** as a dark purple solid (8.0 mg, 0.011 mmol, 17%). R$_f$ = 0.5 in 1:10 EtOH/CH$_2$Cl$_2$. ^{1}H NMR (500 MHz, DMSO-*d*$_6$) δ 8.17 (d, *J* = 6.3 Hz, 6H), 7.67 (s, 2H), 7.62 – 7.59 (m, 6H), 7.10 (s, 2H), 7.01 (d, *J* = 9.3 Hz, 2H), 6.86 (s, 2H), 3.16 (s, 12H), 2.87 – 2.81 (m, 4H), 1.93 – 1.87 (m, 2H). Absorbance (CH$_2$Cl$_2$): 524, 916, 1027 nm. $\varepsilon_{max} = (2.3 \pm 0.1) \times 10^5\ \mathrm{M^{-1}cm^{-1}}$ $(\mathrm{n} = 2, \mathrm{average} \pm \mathrm{range})$. Emission (CH$_2Cl_2$, ex. 900 nm): 1056 nm. HRMS (ESI$^+$) m/z calcd for $C_{44}H_{38}D_2ClN_2O_2^+$ [M$^+$]: 665.2898, found 665.2903; isotopic pattern suggests 72% *d*$_2$-, 15% *d*$_3$- and 12% *d*$_4$-product.

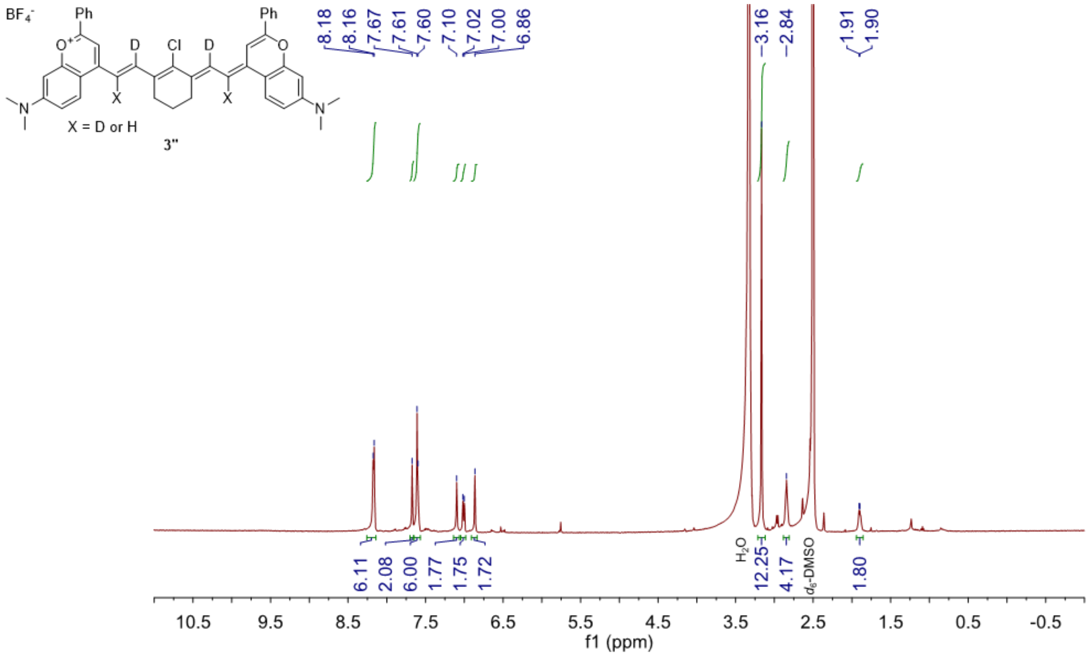

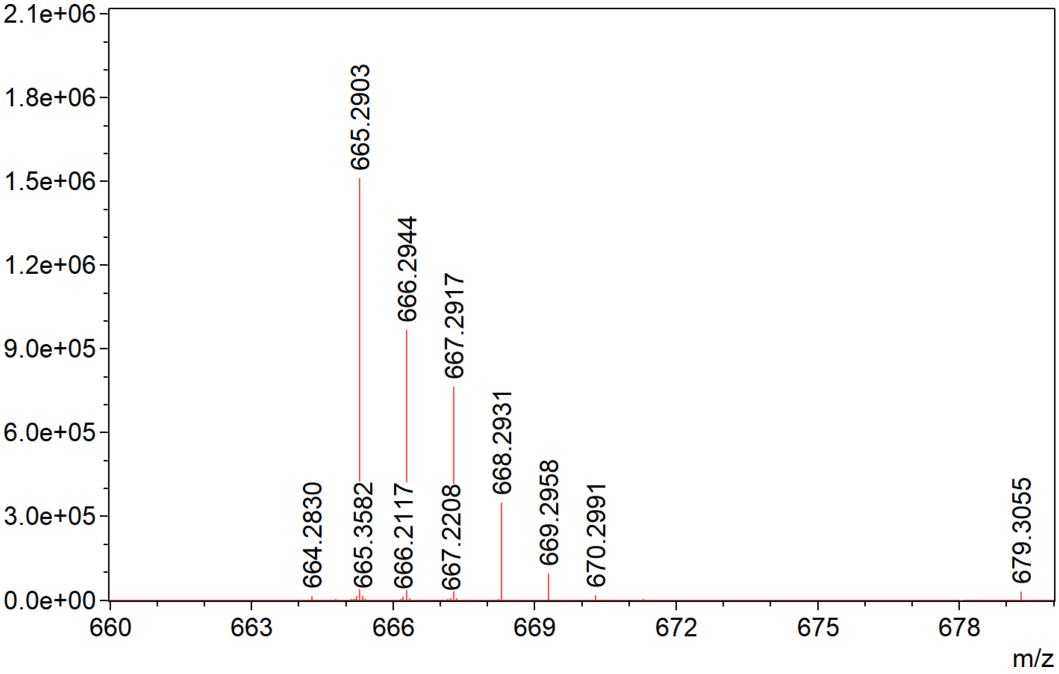

c. Comparison of dyes 3, 3’, and 3” spectral properties

Absorption and emission data to compare how deuteration of the scaffold impacts spectral properties show good overlap near the HOMO-LUMO gap (Figure S10).

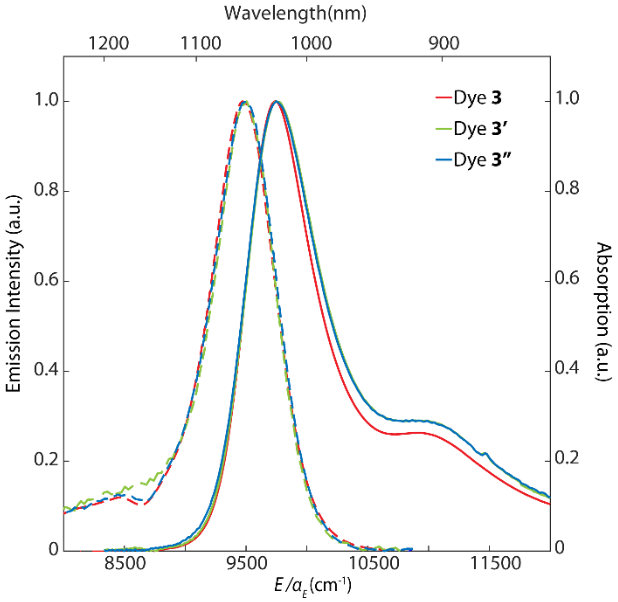

Figure S10: **Steady state spectra of dye 3, 3’, 3”.** Normalized absorption and emission of dye, **3’,** and **3”** show a minimal peak shifting.

d. T-test and error propagation

For all t-tests, we used an independent samples t-test, with different variances. We used a population of one and the assumption that our error propagation in the text was for 95 percent confidence and used only one degree of freedom when converting the t-value. Additionally, for the total rate error, we used the confidence interval from the fitting. Table S3 shows the deviation used for the t-tests.

Table S3: Errors used in t-tests.

Dye	k_{tot} error	k_r error	k_{nr} error
3	3.2×10^7	2.9×10^6	3.2×10^7
3′	3.7×10^7	4.5×10^6	3.7×10^7
3″	4.3×10^7	7.0×10^6	4.4×10^7

VII. 50% quantum yield scaffold comparison

To compare across scaffolds, we numerically solve for when EQME equals 0.5 *e.g.* when $k_{nr} = k_r$. For all points we use $n = 1.5, C = 1000\ cm^{-1}, E_M = 3000\ cm^{-1}$, and $\gamma = 1$. For the other dye classes, we found transition dipole moments using Equation 3. Examples for each chromophore class are shown in Table S4.

Table S4: Values of Other Dye Scaffolds for Comparison Method

Dye Class	**Dye**	$\boldsymbol{\mu_{12}}$	$\boldsymbol{E_{ST}\ (cm^{-1})}$
Squaraines			
	SQA[27]	10.6	190
	SQA2 -r[27]	13.3	100
BODIPY			
	BODIPY 2 Cl[28]	9.9	585
	BODIPY 2O[28]	8.5	571
	BODIPY 2 S[28]	9.2	570
	BODIPY 2Se[28]	9.6	580
	BODIPY 2Te[28]	8.5	776
	PM546 (BODIPY)[11]	7.1	461.4
Fluorescein			
RFL	butyl[29]	8.5	806
	5COOH[29]	8.1	916
	6 COOH[29]	8.1	806
	5 SCN[29]	8.0	1013
	SCN[29]	8.0	973
FLX2	Cl[29]	8.2	840
	Br[29]	8.2	843
	I[29]	8.5	769
	H[29]	8.3	843
FLX4	Cl[29]	8.2	639
	Br[29]	8.5	802
	Br Na Et[29]	8.7	738
	I[29]	8.6	827
R4FLX4	R=Cl X=H[29]	8.6	639
	R=Cl, X=I[29]	8.7	623
	R=Br, X=Cl[29]	9.5	704
	R=H, X=Cl[29]	8.4	639

VIII. Solvent Deuteration Impact on Fluorescence Lifetime.

To analyze O-H overtone stretch impact on lifetime of a SWIR polymethine dye, We took fluorescence lifetimes of IR-1061 in ethanol (EtOH) and ethanol-d1 (EtOD) with 785 laser light (IRF, 80 ps, Figure S11). Deuteration of the O-H stretch increased the lifetime from 14 ± 1 to 25 ± 1 is in part indicative of suppression of nonradiative rate. Quick photodegradation of IR-1061 made relative quantum yield measurements difficult.

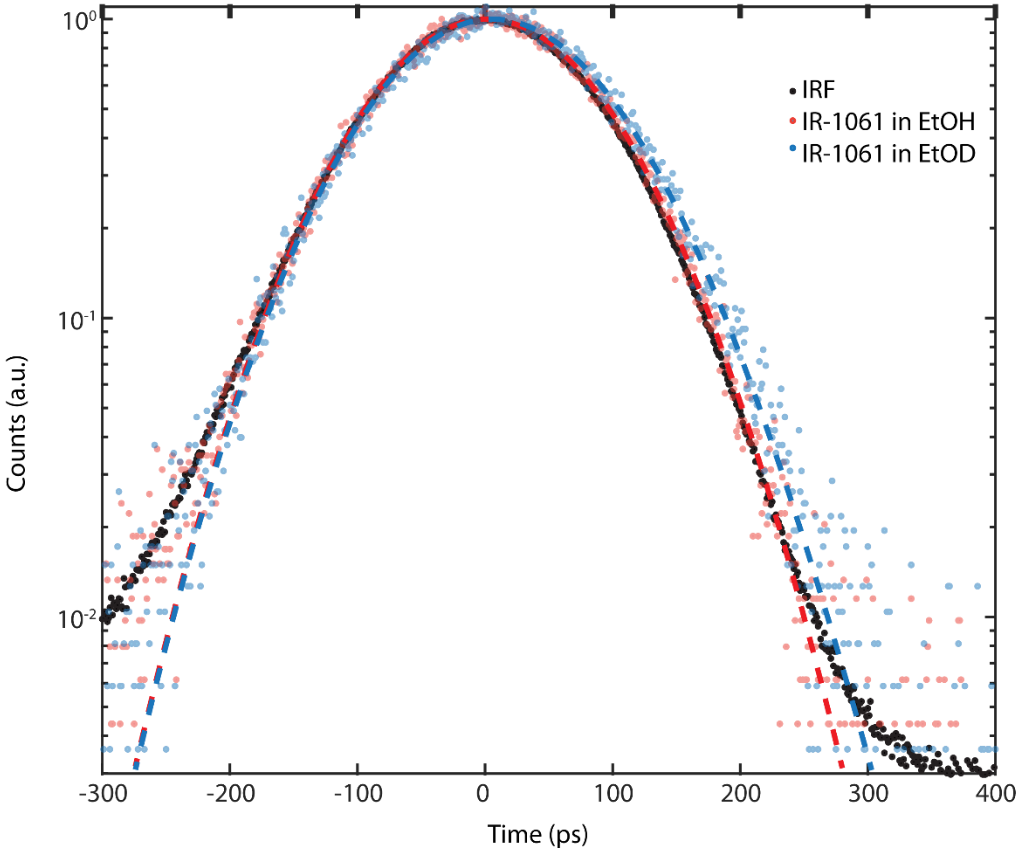

Figure S11: **Impact of Solvent deuteration on fluorescence lifetime:** Fluorescence lifetime of IR-1061 in ethanol and ethanol-d_1

References

1. Cosco, E.D., Spearman, A.L., Ramakrishnan, S., Lingg, J.G.P., Saccomano, M., Pengshung, M., Arús, B.A., Wong, K.C.Y., Glasl, S., Ntziachristos, V., et al. (2020). Shortwave infrared polymethine fluorophores matched to excitation lasers enable non-invasive, multicolour in vivo imaging in real time. Nat. Chem. *12*, 1123–1130.
2. Cosco, E.D., Arús, B.A., Spearman, A.L., Atallah, T.L., Lim, I., Leland, O.S., Caram, J.R., Bischof, T.S., Bruns, O.T., and Sletten, E.M. (2021). Bright Chromenylium Polymethine Dyes Enable Fast, Four-Color in Vivo Imaging with Shortwave Infrared Detection. J. Am. Chem. Soc. *143*, 6836–6846.
3. Cosco, E.D., Caram, J.R., Bruns, O.T., Franke, D., Day, R.A., Farr, E.P., Bawendi, M.G., and Sletten, E.M. (2017). Flavylium Polymethine Fluorophores for Near- and Shortwave Infrared Imaging. Angew. Chemie Int. Ed. *56*, 13126–13129.
4. Semonin, O.E., Johnson, J.C., Luther, J.M., Midgett, A.G., Nozik, A.J., and Beard, M.C. (2010). Absolute photoluminescence quantum yields of IR-26 Dye, PbS, and PbSe quantum dots. J. Phys. Chem. Lett. *1*, 2445–2450.
5. Hatami, S., Würth, C., Kaiser, M., Leubner, S., Gabriel, S., Bahrig, L., Lesnyak, V., Pauli, J., Gaponik, N., Eychmüller, A., et al. (2015). Absolute photoluminescence quantum yields of IR26 and IR-emissive Cd1-xHgxTe and PbS quantum dots-method- and material-inherent challenges. Nanoscale *7*, 133–143.
6. Atallah, T.L., Sica, A. V., Shin, A.J., Friedman, H.C., Kahrobai, Y.K., and Caram, J.R. (2019). Decay-Associated Fourier Spectroscopy: Visible to Shortwave Infrared Time-Resolved Photoluminescence Spectra. J. Phys. Chem. A *123*, 6792–6798.
7. Pengshung, M., Neal, P., Atallah, T.L., Kwon, J., Caram, J.R., Lopez, S.A., and Sletten, E.M. (2020). Silicon incorporation in polymethine dyes. Chem. Commun. *56*, 6110–6113.
8. Hilborn, R.C. (1982). Einstein coefficients, cross sections, f values, dipole moments, and all that. Am. J. Phys. *50*, 982–986.
9. Strickler, S.J., and Berg, R.A. (1962). Relationship between absorption intensity and fluorescence lifetime of molecules. J. Chem. Phys. *37*, 814–822.
10. Hirayama, S., and Phillips, D. (1980). Correction for refractive index in the comparison of radiative lifetimes in vapour and solution phases. J. Photochem. *12*, 139–145.
11. Chung, P.-H., Tregidgo, C., and Suhling, K. (2016). Determining a fluorophore’s transition dipole moment from fluorescence lifetime measurements in solvents of varying refractive index. Methods Appl. Fluoresc. *4*, 045001.
12. Toptygin, D. (2003). Effects of the Solvent Refractive Index and Its Dispersion on the Radiative Decay Rate and Extinction Coefficient of a Fluorescent Solute. J. Fluoresc. *13*, 201–219.
13. Fox, M. (1970). Quantum Optics: An Introduction (Oxford Master Series in Physics).
14. Bixon, M., and Jortner, J. (1968). Intramolecular Radiationless Transitions. J. Chem. Phys. *48*, 715–726.
15. Lin, Z., W. Kohn, A., and Van Voorhis, T. (2020). Toward Prediction of Nonradiative Decay Pathways in Organic Compounds II: Two Internal Conversion Channels in BODIPYs. J. Phys. Chem. C *124*, 3925–3938.
16. Faraji, S., Matsika, S., and Krylov, A.I. (2018). Calculations of non-adiabatic couplings within equation-of-motion coupled-cluster framework: Theory, implementation, and validation against multi-reference methods. J. Chem. Phys. *148*, 044103.
17. Warshel, A., and Dauber, P. (1977). Calculations of resonance Raman spectra of conjugated molecules. J. Chem. Phys. *66*, 5477–5488.
18. Ding, B., Xiao, Y., Zhou, H., Zhang, X., Qu, C., Xu, F., Deng, Z., Cheng, Z., and Hong, X. Polymethine Thiopyrylium Fluorophores with Absorption beyond 1000 nm for Biological Imaging in

the Second Near-Infrared Subwindow. J. Med. Chem. *62*, 2049–2059.

19. Rurack, K., and Spieles, M. (2011). Fluorescence Quantum Yields of a Series of Red and Near-Infrared Dyes Emitting at 600−1000 nm. Anal. Chem. *83*, 1232–1242.
20. Shi, Y., Yuan, W., Liu, Q., Kong, M., Li, Z., Feng, W., Hu, K., and Li, F. (2019). Development of Polyene-Bridged Hybrid Rhodamine Fluorophores for High-Resolution NIR-II Imaging. ACS Mater. Lett., 418–424.
21. Russin, T.J., Altinoğlu, E.İ., Adair, J.H., and Eklund, P.C. (2010). Measuring the fluorescent quantum efficiency of indocyanine green encapsulated in nanocomposite particulates. J. Phys. Condens. Matter *22*, 334217.
22. Lei, Z., Sun, C., Pei, P., Wang, S., Li, D., Zhang, X., and Zhang, F. (2019). Stable, Wavelength-Tunable Fluorescent Dyes in the NIR-II Region for In Vivo High-Contrast Bioimaging and Multiplexed Biosensing. Angew. Chemie - Int. Ed. *58*, 8166–8171.
23. Ayala-Orozco, C., Liu, J.G., Knight, M.W., Wang, Y., Day, J.K., Nordlander, P., and Halas, N.J. (2014). Fluorescence enhancement of molecules inside a gold nanomatryoshka. Nano Lett. *14*, 2926–2933.
24. Li, B., Lu, L., Zhao, M., Lei, Z., and Zhang, F. (2018). An Efficient 1064 nm NIR-II Excitation Fluorescent Molecular Dye for Deep-Tissue High-Resolution Dynamic Bioimaging. Angew. Chemie Int. Ed. *57*, 7483–7487.
25. Wang, S., Fan, Y., Li, D., Sun, C., Lei, Z., Lu, L., Wang, T., and Zhang, F. (2019). Anti-quenching NIR-II molecular fluorophores for in vivo high-contrast imaging and pH sensing. Nat. Commun. *10*, 1058.
26. Li, B., Zhao, M., Feng, L., Dou, C., Ding, S., Zhou, G., Lu, L., Zhang, H., Chen, F., Li, X., et al. (2020). Organic NIR-II molecule with long blood half-life for in vivo dynamic vascular imaging. Nat. Commun. *11*, 3102.
27. Marciniak, H., Auerhammer, N., Ricker, S., Schmiedel, A., Holzapfel, M., and Lambert, C. (2019). Reduction of the Fluorescence Transition Dipole Moment by Excitation Localization in a Vibronically Coupled Squaraine Dimer. J. Phys. Chem. C *123*, 3426–3432.
28. Fron, E., Coutiño-Gonzalez, E., Pandey, L., Sliwa, M., Van Der Auweraer, M., De Schryver, F.C., Thomas, J., Dong, Z., Leen, V., Smet, M., et al. (2009). Synthesis and photophysical characterization of chalcogen substituted BODIPY dyes. New J. Chem. *33*, 1490–1496.
29. Zhang, X.F., Zhang, J., and Liu, L. (2014). Fluorescence properties of twenty fluorescein derivatives: Lifetime, quantum yield, absorption and emission spectra. J. Fluoresc. *24*, 819–826.